On the numerical modeling of laser powder bed fusion additive manufacturing of Ti-6Al-4V

Ali Ghasemi[1], Rasid Ahmed Yildiz[1], Mohammad Malekan[1]

[1] *Centre for Industrial Mechanics, Department of Mechanical and Electrical Engineering, University of Southern Denmark*
Sønderborg, DK-6400, Denmark
alighasemi@sdu.dk, yildizras@sdu.dk, malekan@sdu.dk

Abstract. Laser Powder Bed Fusion (LPBF) represents an additive manufacturing methodology employed to produce intricately designed components. Residual stresses, stemming from the swift thermal transitions inherent in this process, can give rise to defects like cracks, distortions, and delamination. This research endeavors to comprehensively examine the dynamics governing the progression of residual stresses and temperatures during the LPBF of Ti-6Al-4V. A three-dimensional finite element model was developed to investigate the influence of various process parameters on the intricate variations of temperature and stresses throughout multi-layer LPBF procedure, as well as the resultant residual stress post-cooling. The outcomes reveal a substantial influence of process parameters on the temperature gradients and final stress distributions. Notably, higher input energy to the layer led to elevated induced residual stresses. The transition from 50 W to 400 W in laser power resulted in a pronounced shift in residual stress, effecting a transformation from -56 MPa (i.e., compressive) to 148 MPa (i.e., tensile).

Keywords: Laser powder bed fusion, finite element simulation, residual stress, temperature, Ti-6Al-4V.

1 Introduction

Additive manufacturing (AM) has gained significant popularity over the past decade. Among the array of additive manufacturing techniques, Laser Powder Bed Fusion (LPBF) stands out for its capacity to fabricate intricate geometric features. A primary advantage inherent in this technology is the notable reduction in material wastage, a contrast observed when compared to conventional manufacturing methods such as machining. In contrast, LPBF is confronted with several challenges, including residual stresses, deviations in geometric precision, and cracking [1, 2]. These issues are interconnected and influenced by the repetitive thermal cycles engendered by the swiftly moving laser beam in LPBF process. Hence, developing a profound comprehension of the mechanisms underlying issue formation and the subsequent implementation of effective mitigation strategies are imperative for ensuring the production of structurally sound components via LPBF.

The occurrence of residual stress within LPBF arises from the pronounced temperature gradient and the swift cycles of heating and cooling inherent in laser deposition [3]. The cooling rate during solidification is acknowledged to reach remarkable levels, ranging from 10^5 to 10^6 K/s [4]. Furthermore, residual stress is evident at different levels of spatial extent and over varying time frames. At the scale of the melt pool, stress manifests during solidification within a matter of milliseconds. Nonetheless, residual stress is anticipated to undergo ongoing alterations at the component level throughout the entirety of the building process, a duration that may span several hours [5]. Parry, et al. [6] investigated the impact of geometry on residual stress within a selective laser melting process of Titanium alloy. Their findings indicated that the significance of scan strategies diminished when the scan length exceeded 3 mm. Denlinger, et al. [7] developed a three-dimensional nonlinear thermo-mechanical model to assess residual stress and temperature distributions in the LPBF process for a specimen comprising 38 deposited layers. The estimated temperature fields and distortions exhibited close correspondence with experimental measurements, consistently revealing elevated tensile stress levels in freshly deposited layers. Panda and Sahoo [8] conducted a numerical investigation into the impact of laser power and scan speed on stress

development in AlSi10mg. Their findings revealed that altering the laser power from 50 W to 200 W led to stress fluctuations ranging between 86 and 339 MPa, and when the scanning velocity reduced from 100 mm/s to 400 mm/s resulted in stress reduction from 171 to 165 MPa. Zhang et al. [9] employed a fully coupled thermo-mechanical modeling approach to predict the thermal and residual stresses distribution within Ti6Al4V alloy components manufactured using the dual laser beams Powder Bed Fusion-Multi Laser Beam (PBF-MLB) technique by twelve different scanning strategy. The modeling encompassed the utilization of twelve distinct scanning strategies. The outcomes underscore the substantial impact of these scanning strategies on the ultimate residual stress and deformation of the PBF-MLB fabricated components.

Attaining a thorough understanding of multiscale behaviors has proven to be a challenging pursuit, attracting noteworthy interest from both academic research communities and industrial sectors. On the other hand, numerical simulations have the capacity to unveil the formation of residual stress and distribution of temperature at the layer scale. Furthermore, they contribute to deepening our comprehension of how process conditions influence stress formation. Hence, the objective of this study is to assess the impacts of some of the important LPBF process parameters, including the laser beam's power (P) and diameter (D), scanning speed (S), and hatching distance (H), on the distribution of temperature and stresses. The evaluation will focus on the distribution of residual stress and temperature throughout and following the building process, within a structure comprising four deposited layers of Ti-4V-6Al alloy.

2 Numerical modeling of LPBF

A 3D-dimensional coupled thermo-mechanical model was developed using commercial finite element (FE) package Abaqus/standard to simulate LPBF of the four deposited layers of Ti-4V-6Al alloy. This model was used to determine the distribution of stress, residual stress, and temperature. The geometry and FE mesh of the model are illustrated in Figure 1(a). A substrate with dimensions of 2000 × 2000 × 600 µm³ and a deposition region with dimensions of 500 × 500 × 120 µm³ were employed. Uniform meshes were utilized, and the mesh size within the deposition region was set at 30 µm. The laser power of 200W, a scanning speed of 1 m/s, a laser spot diameter of 100 µm, a hatch spacing of 100 µm, the optical penetration of 65 µm, and the layer thickness of 30 µm were employed for LPBF process of Ti6Al4V alloy. The simulation utilized a track wise back-and-forth bidirectional laser scanning strategy with a hatch spacing of 100 µm, as shown in Figure 1(b). Additionally, a rotation of 90 degrees for the scanning paths was applied on a layer-by-layer basis. Convection and radiation heat transfer were both included in the model. The bottom surface of the substrate was constrained, restricting all degrees of freedom.

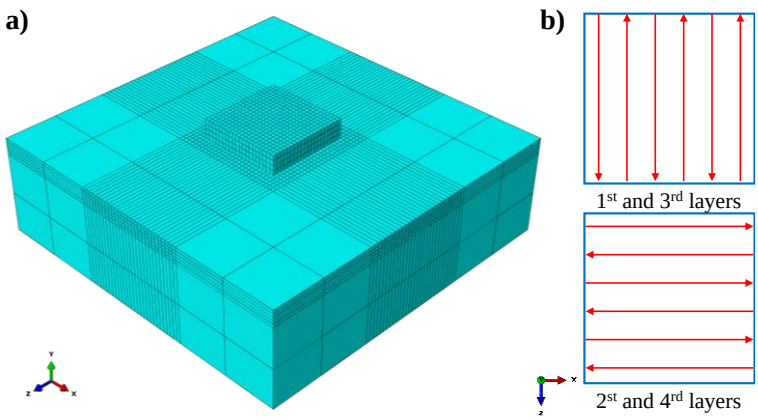

Figure 1 a) 3D finite element meshes of LPBF model and b) scanning strategies utilized for layers 1st to 4th.

In the Abaqus DFLUX subroutine, a Gaussian distribution was implemented to model the heat flux, which is described as:

$$Q = \frac{2AP}{\pi r^2 D} \exp\left(-2\frac{Z^2+X^2}{r^2}\right) \exp\left(\frac{-|Y|}{D}\right). \quad (1)$$

where A, P, r and D denote the laser absorptivity of the powder, the laser power, the beam radius, and the optical penetration depth, respectively [10]. The material properties utilized in this study are provided in Table 1 and Table 2.

Table 1. Physical parameters of Ti-4V-6Al [10, 11].

Parameters	Values
Solidus temperature, T_S (K)	1878
Liquidus temperature, T_L (K)	1928
Thermal conductivity of solid (W $m^{-1}K^{-1}$)	$1.57 + 2.9 \times 10^{-2}T - 7 \times 10^{-6}T^2$
Specific heat of solid (J $kg^{-1}K^{-1}$)	$512.4 + 0.15\ T - 1 \times 10^{-6}T^2$
Emissivity, ε	0.3
Stefan-Boltzmann constant, σ (W m^{-2} K^{-4})	5.67×10^{-8}
Convection coefficient, H (W m^{-2} K^{-1})	10
Laser absorption coefficient	0.3

Table 2. Temperature dependent mechanical properties of Ti-4V-6Al [10, 11].

Temperature (K)	Young's Modulus (GPa)	Poisson's ratio	Thermal expansion coefficient (1/K)	Temperature (K)	Yield stress (Pa)
300	125	0.345	8.76E-06	300	955
533	110	0.35	9.83E-06	573	836
589	100	0.37	1.00E-05	773	732
700	93	0.43	1.07E-05	1023	581
755	80	0.43	1.11E-05	1073	547
811	74	0.43	1.12E-05	1173	480
923	55	0.43	1.17E-05	1273	405
1073	27	0.43	1.22E-05	1373	330
1098	22	0.43	1.23E-05		
1123	18	0.43	1.24E-05		
1573	12	0.43	1.30E-05		
1873	9	0.43	1.63E-05		

3 Results and discussion

The distribution of residual stress and temperature along the paths and versus time in some points, as shown in Figure 2, were extracted from the FE models.

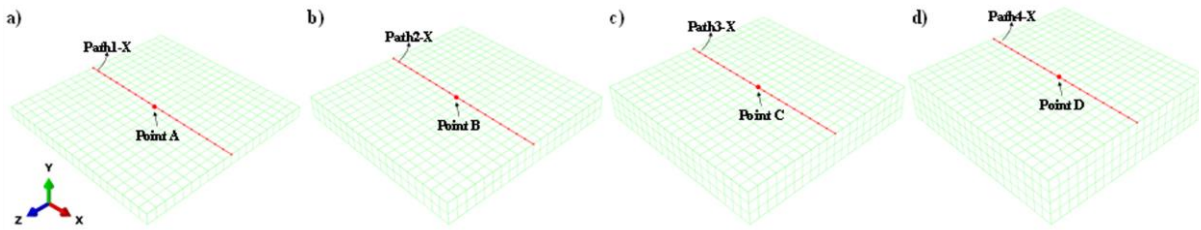

Figure 2: The paths along X direction and the points for different layers including a) 1st layer, b) 2nd layer, c) 3rd layer and d) 4th layer.

3.1 FE validation

For the FE verification, the evolution of stress and temperature at a point within the present FE model was compared to the corresponding FE results obtained from [10], as depicted in Figure 3. The results demonstrate a

noteworthy alignment between the two sets of data. Moreover, these value of temperature was agrees with the experimentally measured values [12] for this alloy. It should be noted that all process parameters, geometric dimensions, and boundary conditions remained consistent with those detailed in the original paper.

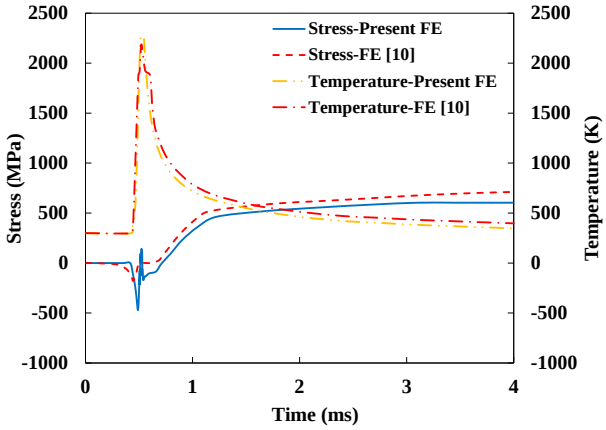

Figure 3: Stress and temperature at a point extracted from the present FE model and from [10].

3.2 Temperature and stress

The temporal evolution of temperature at points A to D during LPBF is illustrated in Figure 4(a). At point A, as the laser approached, the temperature sharply raised and reached its maximum value, then rapidly decreased. With the addition of subsequent layers, the temperature at this point increased sharply as the laser beam passed above this point, but the intensity of the temperature decreased. The maximum temperature also increased for points B, C, and D. This phenomenon can be attributed to the fact that the temperature of the underlying layers was higher than the ambient temperature, and these layers have not had sufficient time to adequately cool down. It should be noted that the thermal cycle depicted in this figure concurred with the experimental measurement values [12]. The stress variations due to LPBF process at points A to D are illustrated in Figure 4(b). This figure effectively depicts the evolution of stress as the laser moves across these points, ultimately leading to the development of residual stresses. Notably, as the laser passed over point A in the first layer, it induced compressive stress, which persisted with the addition of second layer. Upon introducing the third and fourth layers, this compressive stress transformed into tensile stress. The cooling of the sample also contributed to the generation of residual stress. A similar trend is observed for point B. For points C and D, the applied stress followed a similar pattern to the previous cases, but the residual stress at these points was compressive. The presence of both tensile and compressive residual stresses is a result of the establishment of force equilibrium within the additively manufactured specimen.

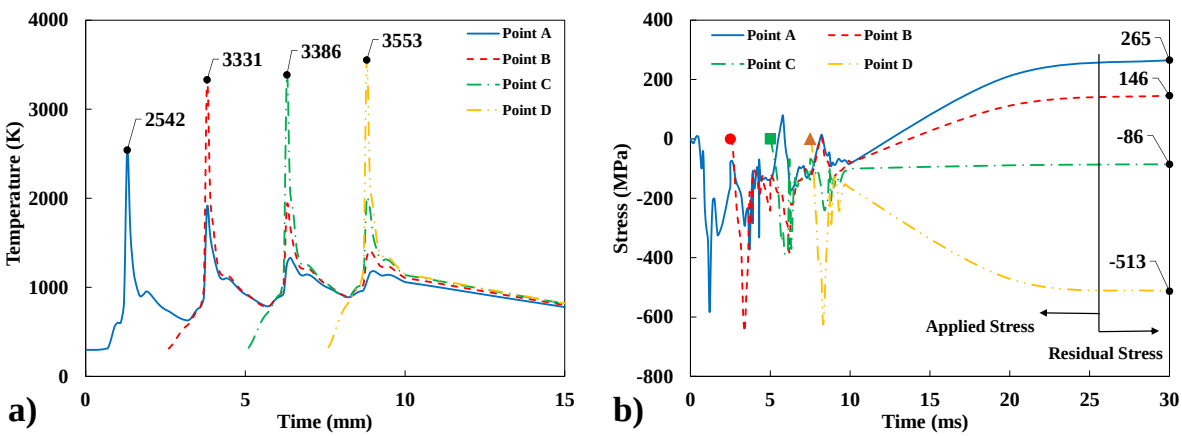

Figure 4: a) the evolution of temperature and b) the evolution of stress and generation residual stress at for different points A to D.

The stress distribution after the addition of each layer and the residual stress after cooling along Path 1-X is shown in Figure 5(a). The highest applied stress was observed during the melting of the 1st layer. Furthermore, the stress maintained compressive following the addition of subsequent layers. However, after the cooling process, a tensile residual stress emerged along this path. In Figure 5(b), show the stress distribution along paths 1 to 4 in X-direction in each layer when scanning was finished on each layer. Eventually, a compressive residual stress was established along Path 4-X after cooling.

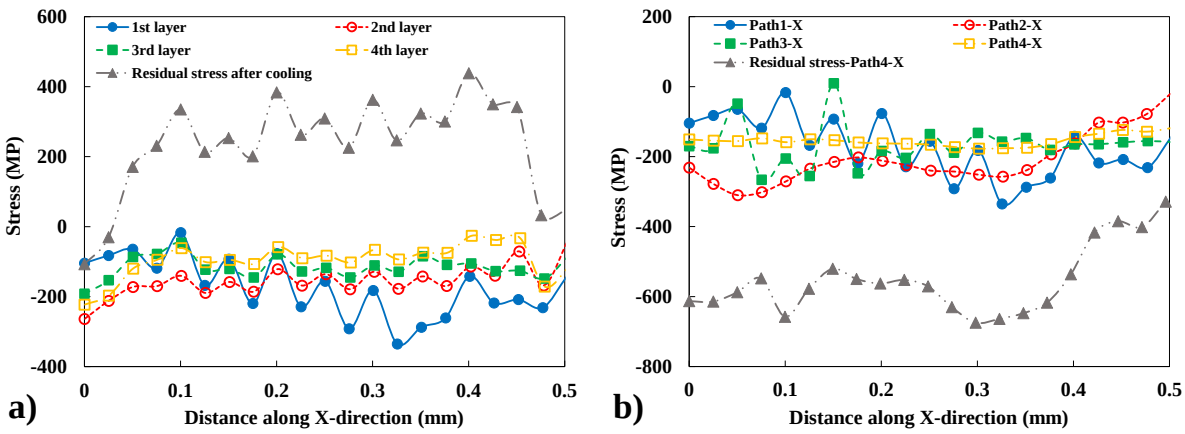

Figure 5: a) applied stress along path1-X after adding each layer and residual stress after cooling and b) applied stress along paths 1 to 4 in X-direction after ending scanning laser on each layer and residual stress along path 4 after cooling.

The effects of different process parameters on temperature and residual stress distribution were investigated. The parameter values were selected as follows: D of 50, 100, and 200 µm; P of 100, 200, and 400 W; H of 50, 100, and 250 µm; and S of 500, 1000, and 2000 mm/s. The temperature contours during the laser scanning of the 4th layer for various process parameters are presented in Figure 6(a) to (i). It is evident that the melting pool expanded along the X-direction for smaller D values. Reducing D concentrated the laser energy into a smaller area, resulting in higher local temperatures and a larger molten pool, as shown in Figure 6(a) to (c). One of the most crucial process parameters is P, which influences the energy input density. This is directly determining the pool temperature and size, as illustrated in Figure 6(d), (b), and (e) corresponding to P = 100, 200, and 400 W. Another influential parameter was H, which impacted the total temperature of the layer during laser scanning. Decreasing H resulted in higher temperatures across the scanned area of the 4th layer, as demonstrated in Figure 6(f) compared to Figure 6(b) and (g). This effect was attributed to the increased energy input rate to each layer as H values decreased. Lastly, the parameter S holds significant influence over the temperature distribution in the fabricated material. Increasing S values lead to reduced energy transfer rates between layers. Figure 6(h) shows that the molten pool and its surrounding temperature are larger for S = 500 mm/s compared to Figure 6(b) and Figure 6(i), where H is 1000 and 2000 mm/s, respectively. Moreover, the effect of D, P, H and S on the average residual stress in the built specimen is depicted Figure 7. It is worth noting that the average residual stress was nearly identical in both the X and Z directions, a phenomenon that can be attributed to the scanning strategy employed in this study. Decreasing D had a good effect on the residual stress, and it change residual stress from tensile to compressive. Increasing P from 50 W to 400 W resulted in an increase in residual stress, shifting it from the compressive value of 56 MPa to a tensile value of 148 MPa. Regarding H, in this study, it can be stated that no significant changes was observed in residual stress by changing H. The trend of the variation of residual stress by S was very similar to D.

The findings underscore the fact that the LPBF fabrication process encounters spatially and temporally diverse stresses. Furthermore, the process parameters play a pivotal role in the generation of residual stresses within the built samples.

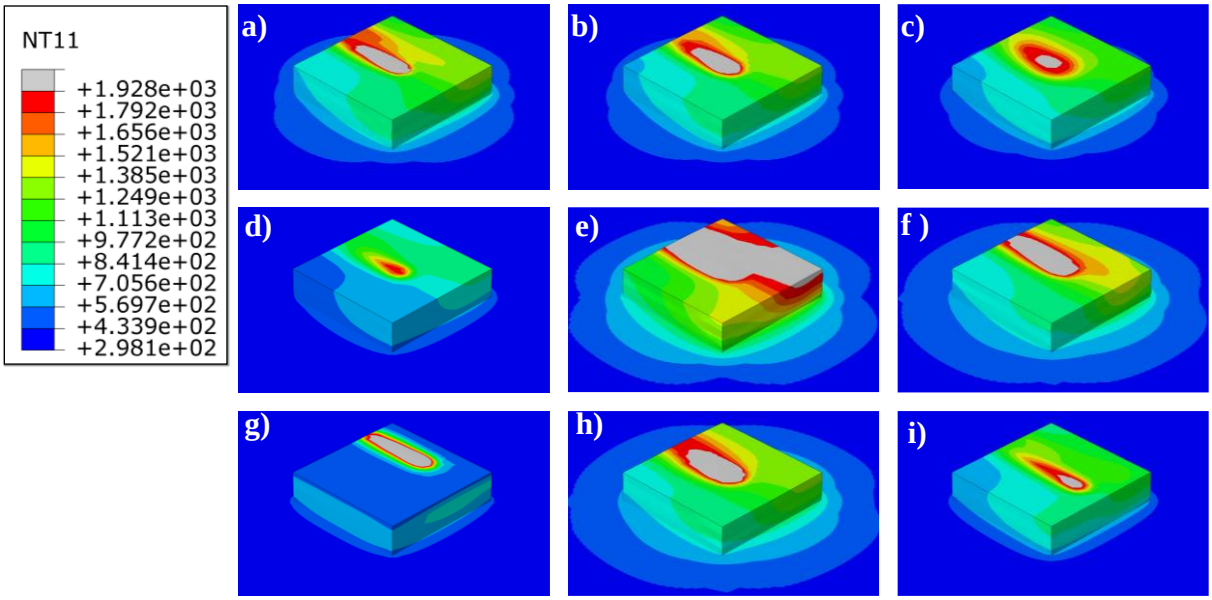

Figure 6: Contour of temperature during melting of the 4th layer for different process parameters: a) D50-P200-H100-S1000, b) D100-P200-H100-S1000, c) D200-P200-H100-S1000, d) D100-P100-H100-S1000, e) D100-P400-H100-S1000, f) D100-P200-H50-S1000, g) D100-P200-H250-S1000, h) D100-P200-H100-S500 and i) D100-P200-H100-S2000.

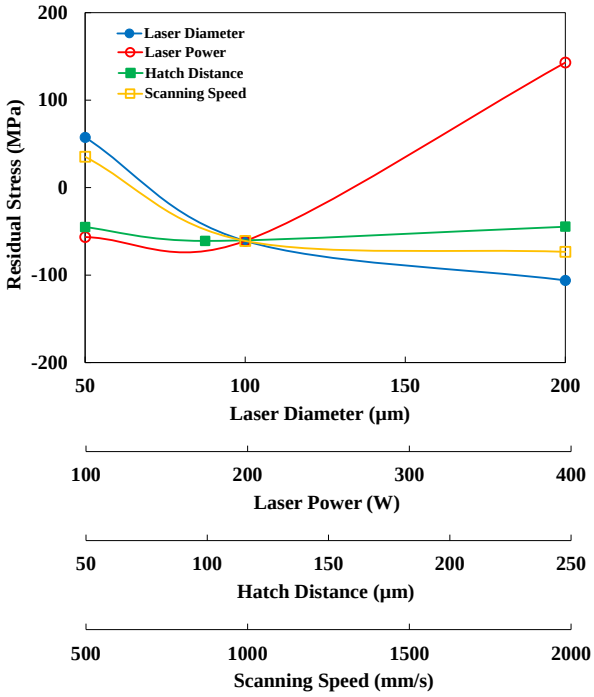

Figure 7: The effect of different process parameters on the average residual stress in the 4 layers after cooling time.

4 Conclusions

This study involves the development of a coupled thermo-mechanical FE model to investigate the spatial and temporal fluctuations of temperature stress, and residual stress during the Laser Powder Bed Fusion (LPBF) process for Ti-6Al-4V. The effect of different parameters of this process on the distribution of temperature, stress, and residual stress during the multi-track and multi-layer deposition procedures was thoroughly investigated. The

following conclusions can be drawn:

- The quantity of input energy delivered by the laser beam onto the surface of the layers determines the temperature level. The parameters that have the potential to augment the input energy directed towards the layers encompass higher laser power and diminished spot size, hatch distance, and scanning speed.
- The higher the temperature of the specimen during this process, the greater the tensile residual stress that was generated in the samples.
- The progression from 50W to 400W in laser power prompted a notable alteration in residual stress, causing a transformation from a compressive state of 56 MPa to a subsequent tensile condition of 148 MPa.

Additional investigations should be carried out with respect to temperature and residual stresses of the AM-built Ti-6Al-4V samples, including real-time imaging via high-speed infrared camera to better tune the FE model, and quantify the level of residual stress via X-Ray diffraction technique. These are among the future studies based on the current work.

Authorship statement. The authors hereby confirm that they are the sole liable persons responsible for the authorship of this work, and that all material that has been herein included as part of the present paper is either the property (and authorship) of the authors or has the permission of the owners to be included here.

References

[1] H.L. Wei, Y. Cao, W.H. Liao, T.T. Liu, Mechanisms on inter-track void formation and phase transformation during laser Powder Bed Fusion of Ti-6Al-4V, Additive Manufacturing, 34, 101221, 2020.

[2] T. DebRoy, T. Mukherjee, H.L. Wei, J.W. Elmer, J.O. Milewski, Metallurgy, mechanistic models and machine learning in metal printing, Nature Reviews Materials, 6, 48-68, 2021.

[3] P. Mercelis, J.P. Kruth, Residual stresses in selective laser sintering and selective laser melting, Rapid Prototyping Journal, 12, 254-265, 2006.

[4] P. Promoppatum, S.-C. Yao, Influence of scanning length and energy input on residual stress reduction in metal additive manufacturing: Numerical and experimental studies, Journal of Manufacturing Processes, 49, 247-259, 2020.

[5] P. Promoppatum, V. Uthaisangsuk, Part scale estimation of residual stress development in laser powder bed fusion additive manufacturing of Inconel 718, Finite Elements in Analysis and Design, 189, 103528, 2021.

[6] L.A. Parry, I.A. Ashcroft, R.D. Wildman, Geometrical effects on residual stress in selective laser melting, Additive Manufacturing, 25, 166-175, 2019.

[7] E.R. Denlinger, M. Gouge, J. Irwin, P. Michaleris, Thermomechanical model development and in situ experimental validation of the Laser Powder-Bed Fusion process, Additive Manufacturing, 16, 73-80, 2017.

[8] B.K. Panda, S. Sahoo, Thermo-mechanical modeling and validation of stress field during laser powder bed fusion of AlSi10Mg built part, Results in Physics, 12, 1372-1381, 2019.

[9] W. Zhang, M. Tong, N.M. Harrison, Scanning strategies effect on temperature, residual stress and deformation by multi-laser beam powder bed fusion manufacturing, Additive Manufacturing, 36, 101507, 2020.

[10] T. Machirori, F.Q. Liu, Q.Y. Yin, H.L. Wei, Spatiotemporal variations of residual stresses during multi-track and multi-layer deposition for laser powder bed fusion of Ti-6Al-4V, Computational Materials Science, 195, 110462, 2021.

[11] T. Mukherjee, W. Zhang, T. DebRoy, An improved prediction of residual stresses and distortion in additive manufacturing, Computational Materials Science, 126, 360-372, 2017.

[12] F. Lia, J.Z. Park, J.S. Keist, S. Joshi, R.P. Martukanitz, Thermal and microstructural analysis of laser-based directed energy deposition for Ti-6Al-4V and Inconel 625 deposits, Materials Science and Engineering: A, 717, 1-10, 2018.